

MATERIALS SCIENCE

A room-temperature ferroelectric semimetal

Pankaj Sharma^{1,2*†}, Fei-Xiang Xiang^{2,3*†}, Ding-Fu Shao^{4*}, Dawei Zhang¹, Evgeny Y. Tsymlal^{4†}, Alex R. Hamilton^{2,3†}, Jan Seidel^{1,2†}

Coexistence of reversible polar distortions and metallicity leading to a ferroelectric metal, first suggested by Anderson and Blount in 1965, has so far remained elusive. Electrically switchable intrinsic electric polarization, together with the direct observation of ferroelectric domains, has not yet been realized in a bulk crystalline metal, although incomplete screening by mobile conduction charges should, in principle, be possible. Here, we provide evidence that native metallicity and ferroelectricity coexist in bulk crystalline van der Waals WTe_2 by means of electrical transport, nanoscale piezoresponse measurements, and first-principles calculations. We show that, despite being a Weyl semimetal, WTe_2 has switchable spontaneous polarization and a natural ferroelectric domain structure at room temperature. This new class of materials has tantalizing potential for functional nanoelectronics applications.

INTRODUCTION

Ferroelectric materials have a spontaneous electric dipole moment, i.e., polarization, even in the absence of an external electric field. This spontaneous electric dipole moment can be repeatedly transitioned between two or more energetically equivalent states or directions upon application of an external electric field that breaks the degeneracy and forms the fundamental underpinning of numerous technological applications of ferroelectric materials (1). For piezoelectricity, noncentrosymmetric crystal structure is the only requirement (2). In contrast, for a polar material, not only must the crystal structure be noncentrosymmetric but also there should exist a unique polar axis. For a material to be considered a ferroelectric, it needs both to be polar and to show bistability of the polarization along the polar axis (2). Conventionally, ferroelectricity has often been associated with and observed in materials that are insulating or semiconducting rather than metallic because conduction electrons in metals screen out the static internal fields arising from a long-range dipolar order. In the 1960s, Anderson and Blount (3) proposed a new class of materials with these seemingly incompatible characteristics, i.e., metals with a polar axis and an inversion asymmetric crystal structure termed “ferroelectric metals.” Since then, an experimental demonstration of this concept for a room-temperature single-phase material has remained elusive. Metallic systems undergoing a centrosymmetric-to-noncentrosymmetric structural transition have been observed recently, e.g., in LiOsO_3 at 140 K (4) and $\text{Cd}_2\text{Re}_2\text{O}_7$ at 200 K (5), hinting at the possibility of sustaining ferroelectricity in a metal at room temperature. More progress has been made lately with a study (6) reporting on the observation of polar domains and strain-induced ferroelastic switching in bulk polar metal $\text{Ca}_3\text{Ru}_2\text{O}_7$ at room temperature. Another strategy that has also been commonly used, besides investigating metallic systems with a noncentrosymmetric crystal structure (7), is to dope well-established ferroelectric materials, such as $\text{BaTiO}_{3-\delta}$ (8, 9) and Nb-doped PbTiO_3

(10). However, the ferroelectric instability weakens with increasing electronic density in these systems and will eventually be destroyed above a certain critical density (11). Furthermore, it is not clear that the ferroelectricity and metallicity coexist in a single phase in these materials (12), as other studies suggest a nanoscale phase separation into separate metallic and ferroelectric phases (13). Another approach to obtaining a ferroelectric metal has been to engineer interface-based polar metals in oxide heterostructures (14–16). Despite these investigations, the experimental realization of a native metal with bistable and electrically switchable spontaneous polarization states, the hallmark of ferroelectricity, is yet to be demonstrated. During the submission process of this manuscript, we became aware of a closely related work (17), in which ferroelectric switching has been demonstrated in device structures through electrical transport measurements for bilayer and trilayer WTe_2 . Fei *et al.* (17) quantify and establish the temperature dependence of the polarization. However, a natural question arises as to whether ferroelectricity persists to samples thicker than three layers, or even to bulk crystals, and whether ferroelectric domains can be formed.

Here, we observe the coexistence of native metallicity and ferroelectricity in bulk crystalline WTe_2 at room temperature. Bulk single crystals in their pristine state show ferroelectric domains that are visualized directly. We demonstrate that the bistable spontaneous ferroelectric polarization state is switchable under an external electrical bias and explain the mechanism for “metallic ferroelectricity” in WTe_2 through a systematic study of the crystal structure, electronic transport measurements, and theoretical considerations. Density functional theory (DFT) calculations show that the ferroelectricity is related to the anisotropy of the crystal structure. A van der Waals material that is both metallic and ferroelectric in its bulk crystalline form at room temperature has potential for new nanoelectronics applications.

RESULTS

Noncentrosymmetric crystal structure and semimetallic ground state

Tungsten ditelluride, WTe_2 , belongs to the class of materials known as transition metal dichalcogenides (TMDCs). These materials exhibit many different crystal structures, such as hexagonal (2H), monoclinic (1T), and orthorhombic (T_d) (18, 19). WTe_2 crystallizes in a layered orthorhombic structure (also known as the T_d phase; Fig. 1A), in which the tungsten atoms are octahedrally coordinated by the tellurium atoms,

Copyright © 2019
The Authors, some
rights reserved;
exclusive licensee
American Association
for the Advancement
of Science. No claim to
original U.S. Government
Works. Distributed
under a Creative
Commons Attribution
NonCommercial
License 4.0 (CC BY-NC).

¹School of Materials Science and Engineering, University of New South Wales, Sydney, NSW 2052, Australia. ²ARC Centre of Excellence in Future Low-Energy Electronics Technologies, University of New South Wales, Sydney, NSW 2052, Australia. ³School of Physics, University of New South Wales, Sydney, NSW 2052, Australia. ⁴Department of Physics and Astronomy and Nebraska Center for Materials and Nanoscience, University of Nebraska, Lincoln, NE 68588-0299, USA.

*These authors contributed equally to this work.

†Corresponding author. Email: pankaj.sharma@unsw.edu.au (P.S.); feixiang.xiang@unsw.edu.au (F.-X.X.); tsymbal@unl.edu (E.Y.T.); alex.hamilton@unsw.edu.au (A.R.H.); jan.seidel@unsw.edu.au (J.S.)

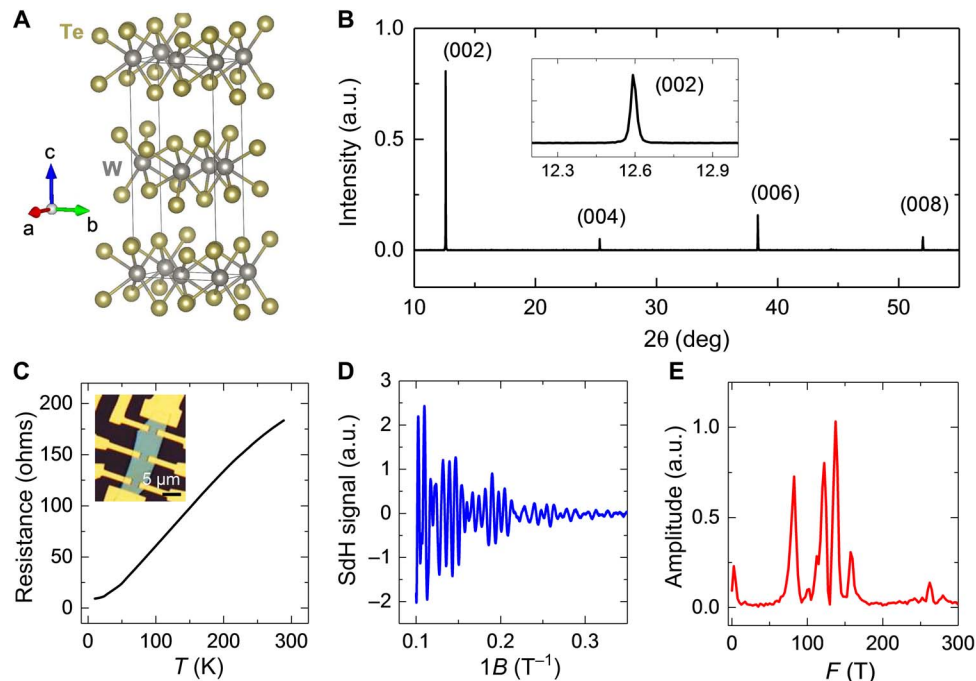


Fig. 1. Crystal and electronic structure of WTe₂. (A) Atomistic model of the T_d phase of WTe₂. (B) XRD θ - 2θ scan on a WTe₂ single crystal. Inset shows a zoom-in on the (002) diffraction peak. a.u., arbitrary units. (C) Temperature-dependent resistance of a WTe₂ sample with a thickness of ~ 50 nm measured from room temperature to 10 K. Inset shows the optical micrograph of the sample. (D and E) SdH oscillations of a WTe₂ sample with a thickness of ~ 30 nm measured at 30 mK (D) and corresponding fast Fourier transform (E).

and the successive layers in between are rotated by 180° (20, 21). Because of strong intermetallic bonding, the tungsten atoms form slightly buckled zigzag chains resulting in distortion of the tellurium octahedra (around each tungsten atom) (19). Figure 1B shows a typical x-ray diffraction (XRD) pattern of c axis-oriented WTe₂ single crystals investigated in this work. The (00l) diffraction peaks confirm the presence of the single-crystalline T_d phase of WTe₂ (20). The lack of inversion symmetry in the T_d phase of WTe₂ (polar space group, $Pmn2_1$) has played an important role in its identification as a type II Weyl semimetal (22). Unlike most TMDCs, WTe₂ is a semimetal in its native ground state (23, 24), instead of being a semiconductor. We confirmed the semimetallic ground state of WTe₂ by electrical transport measurements (Fig. 1C). The resistance of WTe₂ decreases with decreasing temperature from room temperature down to 10 K, a behavior typical of metallic systems. Furthermore, magnetoresistance measurements at 30 mK with magnetic fields up to 10 T reveal pronounced Shubnikov-de Haas (SdH) oscillations with four main frequencies (Fig. 1, D and E). These oscillations confirm the existence of four well-defined Fermi surfaces, consisting of two sets of electron and hole pockets (25). The presence of both free electrons and holes is believed to be the origin of the extremely large, nonsaturated magnetoresistance in WTe₂ (26–28). Given the existence of metallic conduction down to 30 mK, and the fact that noncentrosymmetry is a necessary but insufficient requirement for a material to be ferroelectric, an intriguing question arises: Is semimetallic WTe₂ with a noncentrosymmetric space group ($Pmn2_1$) a ferroelectric (7)?

Ferroelectric domains in single crystals

To address this question and probe ferroelectricity in WTe₂, we used piezoresponse force microscopy (PFM) to spatially map the polar-

ization. PFM is a standard technique used extensively to investigate domain microstructure and dynamics of polarization in classical ferroelectric materials. It exploits the converse piezoelectric effect and detects lattice deformation due to an applied electric field (29, 30). To ensure pristine surfaces for the investigation, we prepared freshly cleaved WTe₂ single-crystal samples (several tens of micrometers thick; Fig. 2, A and B, and see Materials and Methods for details). Measurements were performed in an inert dry N₂ environment at room temperature immediately after the crystals were cleaved. In this experiment, the conductive nanoscale tip acts as a movable top electrical contact. Spectroscopic electrical transport measurements performed using conductive atomic force microscopy (c-AFM) reveal the expected metallic behavior of WTe₂ and establish the ohmic nature of the electrical contacts (see fig. S1). The measured current-bias curves are linear and show appreciable conduction over a rather small bias range. Subsequently, we performed PFM imaging (see Materials and Methods for details). The PFM images (Fig. 2, C to H) show the presence of anti-parallel ferroelectric domains. A few of these domains are visualized in more detail in the high-resolution PFM images (Fig. 2, G and H). The domains usually exhibit a distorted circular profile with an average domain size in the range of ~ 20 to 50 nm. The domain shape resembles those of well-known ferroelectric materials such as strontium bismuth tantalate (29) and triglycine sulfate (31). The piezoresponse characteristics are textbook (29, 32) examples of ferroelectric behavior (Fig. 2, J and K): (i) Domain walls appear as dark lines (i.e., as a minimum in the PFM amplitude signal) in the amplitude image, and (ii) the PFM phase inverts by $\sim 180^\circ$ between adjacent domains in the corresponding phase image. The surface of the sample is atomically flat (root mean square roughness, ~ 0.2 nm) with occasional step edges (Fig. 2C) from the cleaving process. We note that, in some

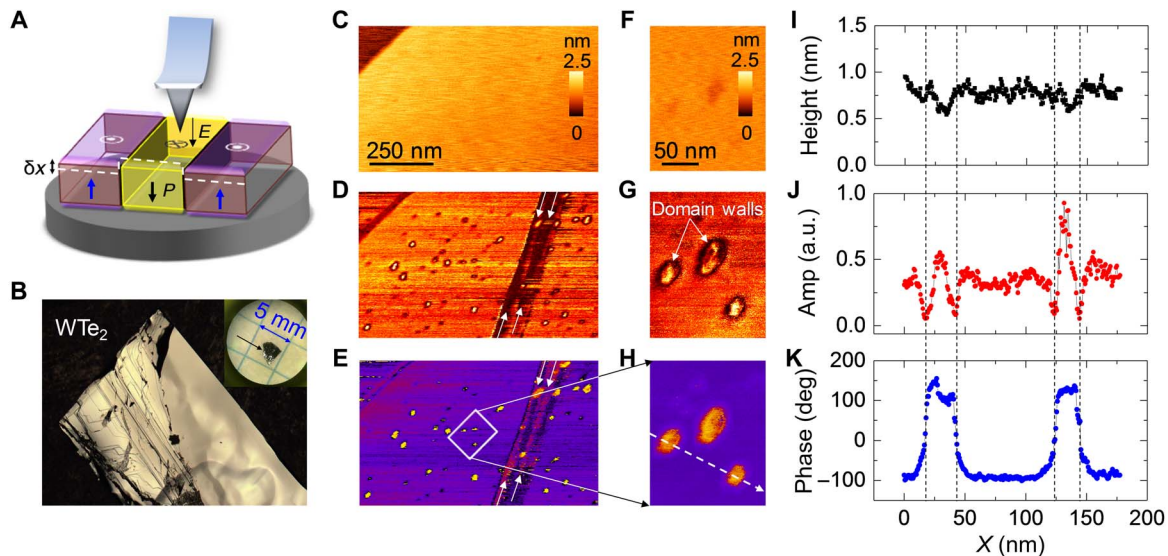


Fig. 2. Ferroelectric domains resolved in WTe₂ single crystals. (A) Schematic of the experimental setup for imaging domains in WTe₂ single crystals. (B) High-magnification optical image of the WTe₂ single crystal sample. Inset shows optical image of a bulk WTe₂ single crystal. (C to E) Topography (C), corresponding PFM amplitude (D), and PFM phase images (E). (F to H) High-magnification imaging of small ferroelectric domains enclosed within the rectangle shown in (E), topography (F), corresponding PFM amplitude (G), and PFM phase images (H). (I to K) Cross-sectional profiles of topography (I), PFM amplitude (J), and phase (K) across the dashed white line shown in (H) for respective images in (F) to (H).

but not all cases, submonolayer surface variations close to the resolution limit of our measurement system were observed near the position of the domains (Fig. 2I). In addition to the small oval domains, micrometer-sized stripe-like domains (shown by arrows in Fig. 2D) were also resolved. This observation of domains in semimetallic WTe₂ single crystals implies that WTe₂ not only has a polar axis (*c* axis) but also has bistable polarization states manifesting as static antiparallel domains. Therefore, the above results strongly support the existence of ferroelectricity in semimetallic WTe₂ at room temperature.

Another aspect that deserves mention here is the stability of WTe₂. It is well known that the surface of WTe₂ is quite sensitive and can undergo oxidation in air. Previous works (33–36) have investigated in detail the physical and chemical properties of this surface oxide using a range of techniques including Raman spectroscopy, energy dispersive x-ray spectroscopy, cross-sectional transmission electron microscopy, x-ray photoelectron spectroscopy, and electrical transport studies. The surface oxide forms through evolution of W–O (WO_x) and Te–O (TeO₂) secondary bonds at the surface of WTe₂ in air. The WTe₂ oxidation is a self-limiting process (35) and results in an amorphous surface oxide layer, which is about 2 nm thick (34). To independently determine time-dependent thickness evolution of the surface oxide, we performed ellipsometry measurements (see section S2 and fig. S2). From our measurements, we find that the thickness of surface oxide saturates at about 2.5 nm after several hours of atmospheric exposure (fig. S2). These results thus are consistent with earlier published reports (34). The exposure time for surface oxide formation ranges from a few hours to days (37). The bulk crystals and relatively thick WTe₂ samples are more stable in air compared to samples with just few layers, especially monolayer and bilayer WTe₂ (35, 36). Moreover, there is no polar space group in amorphous materials, and ferroelectricity cannot arise as it exists only in crystalline materials. This is the very reason that, in the literature, there are no publications reporting on the observation of existing ferroelectric domains or domain-like features using PFM in amorphous materials. Nevertheless, we performed the measurements

presented in Fig. 2 on a freshly cleaved atomically smooth WTe₂ single crystal in a controlled N₂ environment (see also fig. S1), and thus, the observed behavior cannot be ascribed to the surface oxide.

Probing ferroelectricity and polarization switching

One of the defining aspects of ferroelectrics is the reorientation of polarization by means of an external electric field. However, unlike insulating ferroelectrics, switching the polarization is difficult in WTe₂ because of its high conductivity: The applied bias induces electrical current rather than acts on the polar distortion (fig. S1). Nonetheless, if the flow of large electrical currents can be prevented, e.g., by insertion of a dielectric layer between the contacts, then it is possible to apply an electric field to WTe₂ and realize ferroelectric switching. To achieve such a configuration and to preclude the possibility of direct charge injection (30) from the tip into the WTe₂, we prepared thin film samples in a capacitor geometry (Fig. 3A and see Materials and Methods for details). In these capacitor structures, current flow is inhibited by a dielectric layer at the ferroelectric/metal interface (see also section S3) (38), as the WTe₂ sample surface briefly exposed to air before the metal deposition forms a very thin oxide layer (34). Figure 3B shows a metal-gated WTe₂ flake on the surface of a Ti/Au-coated silicon substrate. The WTe₂ flake is 15 nm thick, and the Ti/Au metal electrode on top of it is 9.5 nm thick (Fig. 3B, inset). In this configuration, the electrical current flow across the WTe₂ is strongly suppressed (fig. S3), although the WTe₂ flake is still metallic (25).

To demonstrate switching of the ferroelectric polarization of WTe₂, spectroscopic PFM measurements were performed through the top electrode in a capacitor geometry, which has been successfully used before for subelectrode PFM measurements (29, 30). The acquired piezoresponse as a function of applied bias (Fig. 3, C and D) shows switchable hysteretic behavior consistent with that seen in traditional ferroelectrics such as BaTiO₃ and Pb(Zr_xTi_{1-x})O₃ (32). The PFM amplitude response displays a characteristic “butterfly” curve, while the corresponding phase response exhibits a phase inversion (i.e., a phase

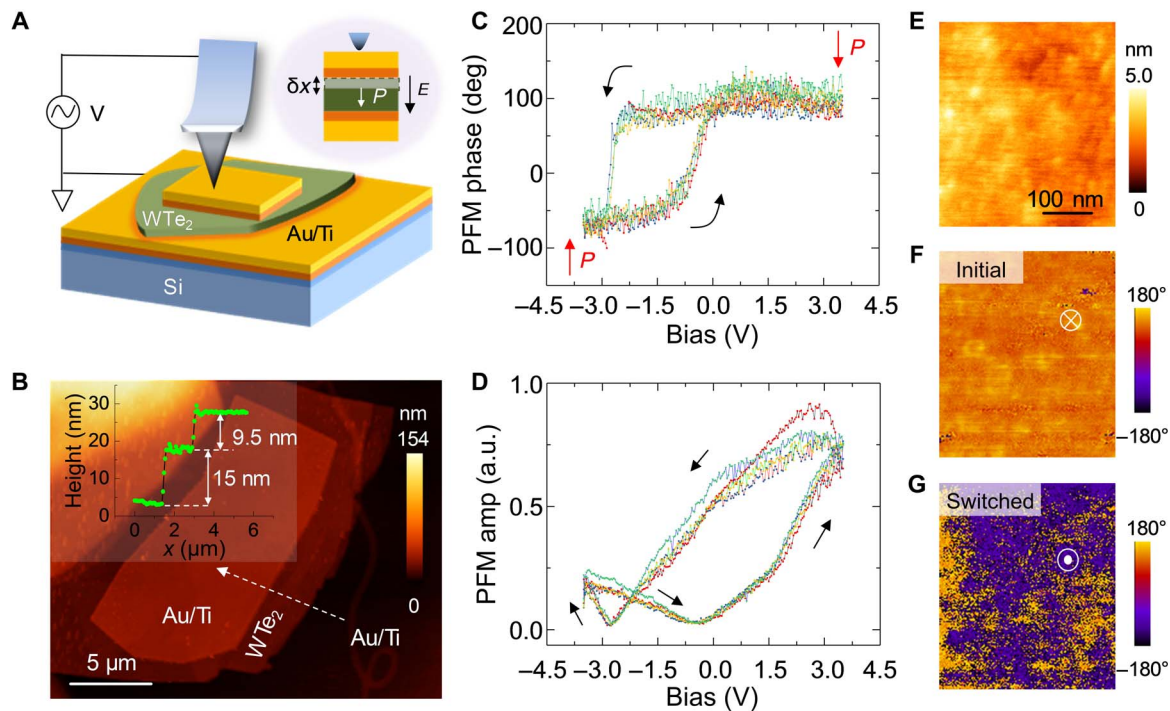


Fig. 3. Probing ferroelectricity in a metal-gated WTe₂ thin film sample. (A) Schematic of the experimental setup and geometry. Inset shows zoomed-in side view of the device structure. (B) Topography image of the metal (Ti/Au)-encapsulated WTe₂ flake on a Si/SiO₂ substrate covered with a conductive buffer layer of Ti/Au. Inset shows the profile of surface morphology along dashed white line. (C and D) Spectroscopic bias-dependent piezoresponse phase (C) and amplitude (D) hysteretic curves acquired through the top metal electrode gating the WTe₂ flake. (E and F) Topography image showing zoom-in on the metal-gated WTe₂ (E) and the corresponding piezoresponse phase image (F). (G) PFM phase image after application of a bias pulse of -2.5 V.

change of approximately 180°) at minima of the amplitude response. To directly visualize these switchable polarization states, we applied switching bias pulses with the subsequent acquisition of PFM images to capture the remnant state. The bias-driven, oppositely oriented remnant polarization can be clearly seen in the PFM images of different color contrasts (Fig. 3, E to G). The initial near-uniform bright contrast of the phase image transforms to a predominant dark phase contrast. This bias-induced transformation between antiparallel equivalent polarization states of the WTe₂ can be accomplished repeatedly and in a reversible fashion by inverting the polarity of the applied writing bias (fig. S4). These measurements therefore demonstrate that the polarization of WTe₂ is switchable under an external bias.

Theoretical insight into the ferroelectric instability

To gain further insight into electronic and structural origins of the ferroelectric instability of WTe₂, we performed first-principles DFT calculations. *T_d*-phase WTe₂ (*T_d*-WTe₂) has a *C_{2v}* point group symmetry, corresponding to the noncentrosymmetric space group *Pmn*2₁. The *C_{2v}* point group contains mirror *ac* and *bc* planes precluding polarization along [100] or [010] direction. The mirror *ab* plane does not belong to this point group and therefore allows for polarization along the [001] direction. Theoretical predictions also show that polar axis orientation can be correlated with electronic anisotropy in layered materials (7). Figure 4A shows the electronic band structure of *T_d*-WTe₂ calculated by DFT (27, 39). The valence band maximum and the conduction band minimum cross the Fermi energy in the Γ -X direction, resulting in the formation of small hole and electron pockets, respectively. The valence band dispersion in the Γ -Z direction is very flat, consistent with nonuniform conduction charge densities in the [001]

direction in Fig. 4B and the anisotropic transport in bulk WTe₂ (40). Therefore, a spontaneous electrical polarization in *T_d*-WTe₂ along the [001] direction is feasible. In a ferroelectric material, the total polarization *P* can be split into contributions from ionic cores (*P_{ion}*) and electrons below *E_F* (*P_{electron}*). In *T_d*-WTe₂, *P_{electron}* can be further split into the contribution of the valence bands (*P_{VB}*), the contribution of the electron pocket (*P_{ep}*), and that of the hole pocket (*P_{hp}*).

Therefore, the total polarization is

$$P = P_{\text{ion}} + P_{\text{electron}} = P_{\text{ion}} + P_{\text{VB}} - P_{\text{hp}} + P_{\text{ep}}$$

P_{ion} + *P_{VB}* dominates the overall effect and is trivial to compute by the Berry phase method (41, 42) with fixed band occupations. We obtain *P_{ion}* + *P_{VB}* = 0.19 $\mu\text{C}/\text{cm}^2$. On the other hand, calculating *P_{hp}* and *P_{ep}* is not standard. Here, we take the method suggested by Filippetti *et al.* (7) to estimate *P_{hp}* and *P_{ep}* by calculating the dipole associated with the conduction electrons. As shown in Fig. 4B, the planar averaged charge density from the electron pocket for each WTe₂ layer is almost symmetric, which does not contribute a dipole. On the other hand, the carriers in the hole pocket contribute a dipole within the layer. However, because of the tiny carrier density, the resulting polarization is negligible (<0.01 $\mu\text{C}/\text{cm}^2$). The total estimated polarization *P* is $\sim 0.19 \mu\text{C}/\text{cm}^2$.

Normally, for a ferroelectric, the opposite (i.e., antiparallel) *P_{up}* and *P_{down}* polarization states can be transformed into one another by application of an inversion operation. The calculated energy barrier for such a transformation in *T_d*-WTe₂ is rather high [0.70 eV/formula unit (f.u.)] (Fig. 4D, top). This is because such a transformation is

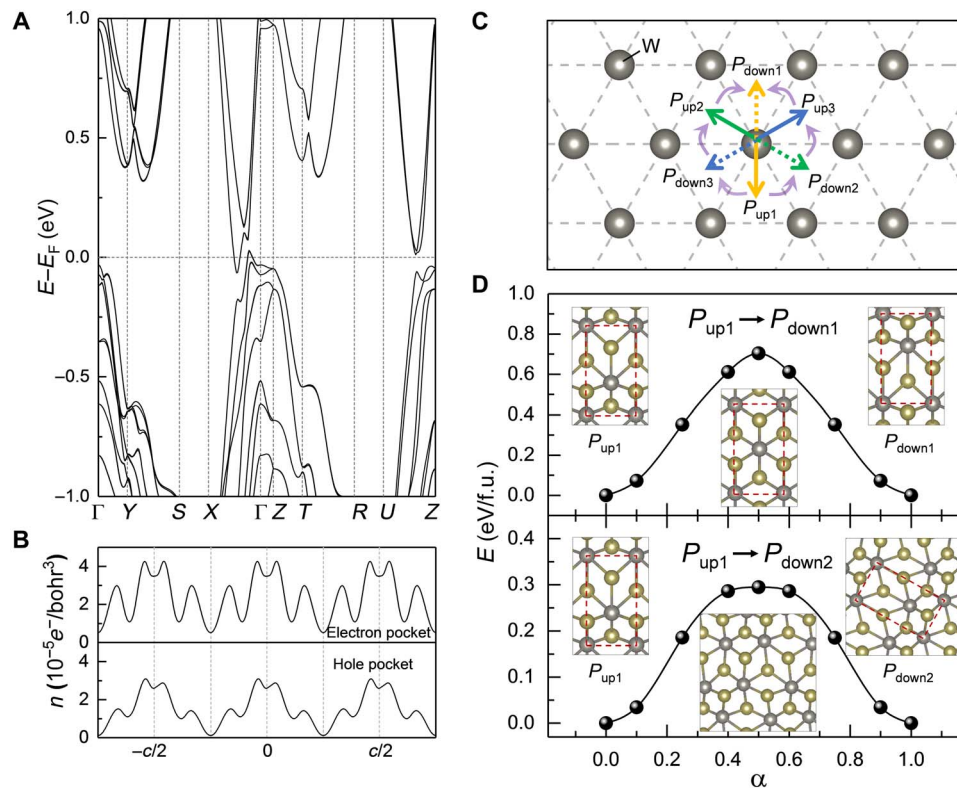


Fig. 4. First-principles DFT calculations. (A) Band structure of T_d -WTe₂. (B) Planar averaged conduction charge densities contributed from the electron pocket (top) and the hole pocket (bottom). (C) Schematic of different distortion vectors in 1T-WTe₂. The solid straight arrows denote three equivalent distortion vectors for the polarization up states (P_{up1} , P_{up2} , and P_{up3}), while the dashed straight arrows denote three equivalent distortions vectors for the polarization down states (P_{down1} , P_{down2} , and P_{down3}). The purple curved arrows denote the possible transition paths from P_{up1} to P_{down1} , involving the switching of different distortion vectors. (D) The energy evolution between opposite polarization states of T_d -WTe₂. The two opposite polarization states (P_{up1} and P_{down1}) are connected by the inversion operation (top), while the polarization down state (P_{down2}) has a different distortion vector, which can be obtained by application of a threefold rotation on P_{down1} (bottom). The energies of intermediate states are calculated using the atomic position $r(\alpha) = r_{up} + \alpha(r_{down} - r_{up})$, where $0 < \alpha < 1$ and r_{up} and r_{down} are the atomic positions of P_{up} and P_{down} , respectively. Insets show the top views of the different states. The red dashed boxes in the insets denote the unit cell of T_d -WTe₂.

associated with a large in-plane lattice displacement. However, the T_d phase is a distorted form of the hexagonal structure with a three-fold rotation symmetry (Fig. 4C). Therefore, there are three equivalent distortion vectors (43). The switching between opposite polarization states with different distortion vectors (i.e., P_{up} of one distortion vector and P_{down} of another distortion vector) should have smaller in-plane atomic displacements on average, leading to a smaller energy barrier. As shown in Fig. 4D (bottom), in this scenario, the energy barrier between opposite polarization states denoted as P_{up1} and P_{down2} is reduced to 0.29 eV/f.u. This value is smaller than (but comparable to) the energy barrier of ~ 0.43 eV/f.u. for BiFeO₃ (44), a prototypical ferroelectric with a high Curie temperature (~ 1000 K). A transition path for polarization switching in WTe₂ with an even lower energy barrier has also been proposed recently (45). Hence, polarization switching in WTe₂ is achievable under normal experimental conditions from a theoretical point of view, supporting the theory that WTe₂ is not only polar but also ferroelectric.

DISCUSSION

Using density functional perturbation theory (46) and the finite differences method (47), we calculated the magnitude of the piezoelectric coefficient of WTe₂ (see table S1 and fig. S5 for details). The calculated value of the longitudinal piezoelectric coefficient (d_{33})

is about 6.5 pm/V. We find that this calculated value is about an order of magnitude larger than the experimentally measured value of ~ 0.7 pm/V (see fig. S6 and corresponding text in section S5). However, the experimentally determined rather low value of the piezoelectric constant is understandable if one were to consider that we likely extract the piezoresponse within the Debye length of WTe₂, which is ~ 1.6 nm (see section S6 for details on the calculation of Debye length). Moreover, the calculation is done for a uniform system, while in the measurements, the electric field distribution is likely highly non-uniform. While the detection of piezoresponse at these small length scales of few nanometers is challenging, it is nevertheless not unrealistic. Furthermore, we are aware of electrically induced extrinsic mechanisms (e.g., electrostatic effects and/or electrochemical processes) that can manifest as a piezoelectric- or a ferroelectric-like effect in PFM studies of nominally nonferroelectric materials. However, the experimental data in the present study of WTe₂ cannot be explained by these spurious extrinsic mechanisms (see section S7 for a detailed discussion). We note that the Debye length of ~ 1.6 nm is relatively short compared to the material thicknesses investigated in our study. Nevertheless, one can obtain depth-sensitive data from electrical measurements for thicknesses larger than the Debye length in WTe₂ (48). In our study, we have observed ferroelectric domains in thick bulk crystals and ferroelectric switching in ~ 15 -nm films. The question of the physical extent of these

domains is an interesting one. One possibility is that the piezoresponse and ferroelectric domains come only from within a Debye length of the surface. However, it is also possible that the ferroelectric domains extend much deeper into the material because ferroelectricity and ferroelasticity are often coupled in conventional ferroelectrics and because ferroelastic domains have been predicted for bulk WTe_2 (43). In this latter scenario, ferroelectric domains could potentially propagate through elastically mediated wall motion, where fluctuation in bond lengths by electric fields initiated on the surface (within the Debye length) generates strain down into the bulk of the material and large domains could propagate through into the depth of the material (6). We hope that our study will stimulate further theoretical and experimental studies to answer this question.

In summary, the concept of ferroelectric metals predicted in the 1960s has been realized in a Weyl semimetal, WTe_2 . A combination of experimental and first-principles DFT techniques demonstrates the coexistence of native metallicity and ferroelectricity at room temperature. Bulk crystalline WTe_2 exhibits bistable polarization states that are switchable under an external electric field—thus, ferroelectricity is a bulk property of WTe_2 —and is not just confined to few-layer samples. The investigation of ferroelectric domain walls (49, 50) in metallic systems constitutes an interesting aspect for future research and potential nanoelectronics applications, following recent findings in conventional ferroelectrics. Our findings also raise prospects for discovering ferroelectricity in other metallic layered materials.

MATERIALS AND METHODS

Sample fabrication details

All WTe_2 samples were prepared from bulk crystals purchased from HQ Graphene, The Netherlands (www.hqgraphene.com). For the PFM measurements on bulk samples, the WTe_2 single crystals were first mounted on a metal disc using conductive Ag paste. To ensure a pristine surface for the measurements, the WTe_2 single crystals were cleaved using the Scotch tape method. For measurements on WTe_2 thin samples in a capacitor geometry, we first deposited 15 nm Ti/Au on the SiO_2 surface of the doped Si substrates. The WTe_2 thin flakes exfoliated from the bulk crystals were then transferred onto the substrates and were covered by poly(methyl methacrylate). Thereafter, electron beam lithography was used to pattern the area for subsequent metal deposition (10 nm Ti/Au). To remove any residual resist and control the surface oxides on the WTe_2 sample, the patterned areas were briefly etched with an Ar plasma. The cleaned surface was exposed to air for ~10 min before loading into the vacuum chamber for the metal deposition, so that only a very thin oxide layer was formed at the surface.

XRD characterization

XRD θ -2 θ scans were performed with a PANalytical X'Pert Pro diffractometer using $\text{Cu K}\alpha$ -1 radiation.

Electrical transport measurements

The temperature-dependent resistance of WTe_2 was measured in a home-built variable temperature system. The SdH oscillations were measured in an Oxford dilution fridge with a base temperature of 30 mK and magnetic fields up to 10 T. The magnetic field direction was perpendicular to the ab plane of the WTe_2 sample.

Scanning probe microscopy measurements

The scanning probe microscopy measurements were implemented on a commercial AIST-NT SmartSPM 1000 atomic force microscope at room

temperature in an inert atmosphere (i.e., controlled N_2 environment). The PFM measurements were performed at an AC imaging bias of 1 V (peak to peak) and a frequency of approximately 700 kHz. The spectroscopic piezoresponse hysteresis loops were acquired at fixed spatial locations by supplying a triangular DC waveform with a superimposed low-amplitude AC modulation.

Ellipsometry measurements

The ellipsometry measurements to determine surface oxide thickness were performed using a variable-angle spectroscopic ellipsometry system (J.A. Woollam Co. Inc.) under ambient conditions. The incident angle of light used in the study was 70°, and the wavelength range was from 300 to 2000 nm with wavelength increments of 10 nm.

First-principles DFT calculations

First-principles DFT calculations have been performed using Quantum ESPRESSO (51) and Vienna Ab initio Simulation Package (VASP) (52, 53). In Quantum ESPRESSO, the optimized norm-conserving Vanderbilt pseudopotentials (54, 55) were used. In VASP, the projector augmented wave method (56) was used. The exchange and correlation effects were treated within the generalized gradient approximation (57). The lattice constant and atomic coordinates were relaxed until the force on each atom was less than 0.001 eV/Å. For the calculation of bulk WTe_2 , we used a $16 \times 12 \times 8$ k -point mesh in the irreducible Brillouin zone. Spin-orbit coupling was included in the electronic structure calculations. For the simulation of WTe_2 with different distortion vectors, we used supercells ($2 \times 2\sqrt{3}$) of a monolayer and a k -point mesh (12 by 8 by 1). We used the lattice constants and atomic positions of the supercells reported in (43) as the initial input for the structure relaxation.

SUPPLEMENTARY MATERIALS

Supplementary material for this article is available at <http://advances.sciencemag.org/cgi/content/full/5/7/eaax5080/DC1>

Section S1. Electrical transport behavior of WTe_2 single-crystal samples in c-AFM

Section S2. Ellipsometry measurements on a WTe_2 single-crystal

Section S3. Electrical transport behavior of WTe_2 thin films in a capacitor geometry

Section S4. Polarization switching in the metal-gated WTe_2 thin film sample

Section S5. Piezoelectric coefficient of WTe_2

Section S6. Calculation of Debye length of WTe_2

Section S7. Extrinsic mechanisms as the origin of PFM response in WTe_2 ?

Table S1. The calculated piezoelectric constant e_{31} (C/m²) and d_{31} (pm/V) for WTe_2 with a polarization along + z direction.

Fig. S1. Spectroscopic current-bias curves recorded in c-AFM mode on a pristine surface of a freshly cleaved WTe_2 single-crystal sample in a controlled N_2 environment.

Fig. S2. Ellipsometry measurements determining the thickness of the surface oxide on WTe_2 .

Fig. S3. Current-bias characteristics of metal-gated WTe_2 thin film samples.

Fig. S4. Polarization switching in a metal-gated WTe_2 thin film sample.

Fig. S5. The polarization change ΔP with respect to the strain ξ along z direction.

Fig. S6. The calibrated piezoresponse measurements versus bias for a metal-gated WTe_2 thin film sample.

Fig. S7. Stable ferroelectric domains in a WTe_2 single crystal.

References (58–62)

REFERENCES AND NOTES

1. M. E. Lines, A. M. Glass, *Principles and Applications of Ferroelectrics and Related Materials* (Oxford Univ. Press, 1977).
2. P. S. Halasyamani, K. R. Poeppelmeier, Noncentrosymmetric oxides. *Chem. Mater.* **10**, 2753–2769 (1998).
3. P. W. Anderson, E. I. Blount, Symmetry considerations on martensitic transformations: “ferroelectric” metals? *Phys. Rev. Lett.* **14**, 217–219 (1965).

4. Y. Shi, Y. Guo, X. Wang, A. J. Princep, D. Khalyavin, P. Manuel, Y. Michiue, A. Sato, K. Tsuda, S. Yu, M. Arai, Y. Shirako, M. Akaogi, N. Wang, K. Yamaura, A. T. Boothroyd, A ferroelectric-like structural transition in a metal. *Nat. Mater.* **12**, 1024–1027 (2013).
5. I. A. Sergienko, V. Keppens, M. McGuire, R. Jin, J. He, S. H. Curnoe, B. C. Sales, P. Blaha, D. J. Singh, K. Schwarz, D. Mandrus, Metallic “ferroelectricity” in the pyrochlore $\text{Cd}_2\text{Re}_2\text{O}_7$. *Phys. Rev. Lett.* **92**, 065501 (2004).
6. S. Lei, M. Gu, D. Puggioni, G. Stone, J. Peng, J. Ge, Y. Wang, B. Wang, Y. Yuan, K. Wang, Z. Mao, J. M. Rondinelli, V. Gopalan, Observation of quasi-two-dimensional polar domains and ferroelastic switching in a metal, $\text{Ca}_3\text{Ru}_2\text{O}_7$. *Nano Lett.* **18**, 3088–3095 (2018).
7. A. Filippetti, V. Fiorentini, F. Ricci, P. Delugas, J. Íñiguez, Prediction of a native ferroelectric metal. *Nat. Commun.* **7**, 11211 (2016).
8. T. Kolodiaznyy, M. Tachibana, H. Kawaji, J. Hwang, E. Takayama-Muromachi, Persistence of ferroelectricity in BaTiO_3 through the insulator-metal transition. *Phys. Rev. Lett.* **104**, 147602 (2010).
9. Y. Wang, X. Liu, J. D. Burton, S. S. Jaswal, E. Y. Tsymlar, Ferroelectric instability under screened coulomb interactions. *Phys. Rev. Lett.* **109**, 247601 (2012).
10. J.-x. Gu, K.-j. Jin, C. Ma, Q.-h. Zhang, L. Gu, C. Ge, J.-s. Wang, C. Wang, H.-z. Guo, G.-z. Yang, Coexistence of polar distortion and metallicity in $\text{PbTi}_{1-x}\text{Nb}_x\text{O}_3$. *Phys. Rev. B* **96**, 165206 (2017).
11. Y. Iwazaki, T. Suzuki, Y. Mizuno, S. Tsuneyuki, Doping-induced phase transitions in ferroelectric BaTiO_3 from first-principles calculations. *Phys. Rev. B* **86**, 241103 (2012).
12. N. A. Benedek, T. Birol, ‘Ferroelectric’ metals reexamined: fundamental mechanisms and design considerations for new materials. *J. Mater. Chem. C* **4**, 4000–4015 (2016).
13. I.-K. Jeong, S. Lee, S.-Y. Jeong, C. J. Won, N. Hur, A. Llobet, Structural evolution across the insulator-metal transition in oxygen-deficient $\text{BaTiO}_{3-\delta}$ studied using neutron total scattering and Rietveld analysis. *Phys. Rev. B* **84**, 064125 (2011).
14. X.-Z. Lu, J. M. Rondinelli, Epitaxial-strain-induced polar-to-nonpolar transitions in layered oxides. *Nat. Mater.* **15**, 951–955 (2016).
15. T. H. Kim, D. Puggioni, Y. Yuan, L. Xie, H. Zhou, N. Campbell, P. J. Ryan, Y. Choi, J.-W. Kim, J. R. Patzner, S. Ryu, J. P. Podkaminer, J. Irwin, Y. Ma, C. J. Fennie, M. S. Rzchowski, X. Q. Pan, V. Gopalan, J. M. Rondinelli, C. B. Eom, Polar metals by geometric design. *Nature* **533**, 68–72 (2016).
16. Y. Cao, Z. Wang, S. Y. Park, Y. Yuan, X. Liu, S. M. Nikitin, H. Akamatsu, M. Kareev, S. Middey, D. Meyers, P. Thompson, P. J. Ryan, P. Shafer, A. N’Diaye, E. Arenholz, V. Gopalan, Y. Zhu, K. M. Rabe, J. Chakhalian, Artificial two-dimensional polar metal at room temperature. *Nat. Commun.* **9**, 1547 (2018).
17. Z. Fei, W. Zhao, T. A. Palomaki, B. Sun, M. K. Miller, Z. Zhao, J. Yan, X. Xu, D. H. Cobden, Ferroelectric switching of a two-dimensional metal. *Nature* **560**, 336–339 (2018).
18. J. A. Wilson, A. D. Yoffe, The transition metal dichalcogenides discussion and interpretation of the observed optical, electrical and structural properties. *Adv. Phys.* **18**, 193–335 (1969).
19. J. Heising, M. G. Kanatzidis, Structure of restacked MoS_2 and WS_2 elucidated by electron crystallography. *J. Am. Chem. Soc.* **121**, 638–643 (1999).
20. B. E. Brown, The crystal structures of WTe_2 and high-temperature MoTe_2 . *Acta Crystallogr.* **20**, 268–274 (1966).
21. W. G. Dawson, D. W. Bullett, Electronic structure and crystallography of MoTe_2 and WTe_2 . *J. Phys. C Solid State Phys.* **20**, 6159–6174 (1987).
22. A. A. Soluyanov, D. Gresch, Z. Wang, Q. Wu, M. Troyer, X. Dai, B. A. Bernevig, Type-II Weyl semimetals. *Nature* **527**, 495–498 (2015).
23. S. Kabashima, Electrical properties of tungsten-ditelluride WTe_2 . *J. Phys. Soc. Jpn.* **21**, 945–948 (1966).
24. J. Augustin, V. Eyert, T. Böker, W. Frentrop, H. Dwell, C. Janowitz, R. Manzke, Electronic band structure of the layered compound $\text{Td}-\text{WTe}_2$. *Phys. Rev. B* **62**, 10812–10823 (2000).
25. F.-X. Xiang, A. Srinivasan, Z. Z. Du, O. Klocan, S.-X. Dou, A. R. Hamilton, X.-L. Wang, Thickness-dependent electronic structure in WTe_2 thin films. *Phys. Rev. B* **98**, 035115 (2018).
26. I. Pletikosić, M. N. Ali, A. V. Fedorov, R. J. Cava, T. Valla, Electronic structure basis for the extraordinary magnetoresistance in WTe_2 . *Phys. Rev. Lett.* **113**, 216601 (2014).
27. M. N. Ali, J. Xiong, S. Flynn, J. Tao, Q. D. Gibson, L. M. Schoop, T. Liang, N. Haldolaarachchige, M. Hirschberger, N. P. Ong, R. J. Cava, Large, non-saturating magnetoresistance in WTe_2 . *Nature* **514**, 205–208 (2014).
28. F.-X. Xiang, M. Veldhorst, S.-X. Dou, X.-L. Wang, Multiple Fermi pockets revealed by Shubnikov-de Haas oscillations in WTe_2 . *Europhys. Lett.* **112**, 37009 (2015).
29. S. V. Kalinin, A. Gruverman, *Scanning Probe Microscopy: Electrical and Electromechanical Phenomena at the Nanoscale* (Springer Science & Business Media, 2007).
30. P. Sharma, J. Seidel, Scanning Probe Microscopy of Functional Materials Surfaces and Interfaces, in *Advanced Materials Interfaces*, A. Tiwari, H. K. Patra, X. Wang, Eds. (Scrivener Publishing, 2016), pp. 63–125.
31. L. Wehmeier, T. Kämpfe, A. Häußmann, L. M. Eng, In situ 3D observation of the domain wall dynamics in a triglycine sulfate single crystal upon ferroelectric phase transition. *Phys. Status Solidi Rapid Res. Lett.* **11**, 1700267 (2017).
32. S. V. Kalinin, A. Gruverman, Piezoresponse force microscopy and recent advances in nanoscale studies of ferroelectrics, in *Frontiers of ferroelectricity*, S. B. Lang, H. L. Chan, Eds. (Springer, 2007), pp. 107–116.
33. C.-H. Lee, E. C. Silva, L. Calderin, M. A. T. Nguyen, M. J. Hollander, B. Bersch, T. E. Mallouk, J. A. Robinson, Tungsten ditelluride: A layered semimetal. *Sci. Rep.* **5**, 10013 (2015).
34. J. M. Woods, J. Shen, P. Kumaravel, Y. Pang, Y. Xie, G. A. Pan, M. Li, E. I. Altman, L. Lu, J. J. Cha, Suppression of magnetoresistance in thin WTe_2 flakes by surface oxidation. *ACS Appl. Mater. Interfaces* **9**, 23175–23180 (2017).
35. F. Ye, J. Lee, J. Hu, Z. Mao, J. Wei, P. X.-L. Feng, Environmental instability and degradation of single and few-layer WTe_2 nanosheets in ambient conditions. *Small* **12**, 5802–5808 (2016).
36. Y. Kim, Y. I. Jhon, J. Park, J. H. Kim, S. Lee, Y. M. Jhon, Anomalous Raman scattering and lattice dynamics in mono- and few-layer WTe_2 . *Nanoscale* **8**, 2309–2316 (2016).
37. L. Wang, I. Gutiérrez-Lezama, C. Barreteau, N. Ubrig, E. Giannini, A. F. Morpurgo, Tuning magnetotransport in a compensated semimetal at the atomic scale. *Nat. Commun.* **6**, 8892 (2015).
38. M. Stengel, D. Vanderbilt, N. A. Spaldin, Enhancement of ferroelectricity at metal–oxide interfaces. *Nat. Mater.* **8**, 392–397 (2009).
39. H. Y. Lv, W. J. Lu, D. F. Shao, Y. Liu, S. G. Tan, Y. P. Sun, Perfect charge compensation in WTe_2 for the extraordinary magnetoresistance: From bulk to monolayer. *Europhys. Lett.* **110**, 37004 (2015).
40. L. R. Thoutam, Y. L. Wang, Z. L. Xiao, S. Das, A. Luican-Mayer, R. Divan, G. W. Crabtree, W. K. Kwok, Temperature-dependent three-dimensional anisotropy of the magnetoresistance in WTe_2 . *Phys. Rev. Lett.* **115**, 046602 (2015).
41. R. D. King-Smith, D. Vanderbilt, Theory of polarization of crystalline solids. *Phys. Rev. B* **47**, 1651–1654 (1993).
42. R. Resta, Macroscopic polarization in crystalline dielectrics: The geometric phase approach. *Rev. Mod. Phys.* **66**, 899–915 (1994).
43. W. Li, J. Li, Ferroelasticity and domain physics in two-dimensional transition metal dichalcogenide monolayers. *Nat. Commun.* **7**, 10843 (2016).
44. P. Ravindran, R. Vidy, A. Kjekshus, H. Fjellvåg, O. Eriksson, Theoretical investigation of magnetoelectric behavior in BiFeO_3 . *Phys. Rev. B* **74**, 224412 (2006).
45. Q. Yang, M. Wu, J. Li, Origin of two-dimensional vertical ferroelectricity in WTe_2 bilayer and multilayer. *J. Phys. Chem. Lett.* **9**, 7160–7164 (2018).
46. M. Gajdoš, K. Hummer, G. Kresse, J. Furthmüller, F. Bechstedt, Linear optical properties in the projector-augmented wave methodology. *Phys. Rev. B* **73**, 045112 (2006).
47. Y. Le Page, P. Saxe, Symmetry-general least-squares extraction of elastic data for strained materials from ab initio calculations of stress. *Phys. Rev. B* **65**, 104104 (2002).
48. L. Wang, I. Gutiérrez-Lezama, C. Barreteau, D.-K. Ki, E. Giannini, A. F. Morpurgo, Direct observation of a long-range field effect from gate tuning of nonlocal conductivity. *Phys. Rev. Lett.* **117**, 176601 (2016).
49. G. Catalan, J. Seidel, R. Ramesh, J. F. Scott, Domain wall nanoelectronics. *Rev. Mod. Phys.* **84**, 119–156 (2012).
50. J. Seidel, *Topological Structures in Ferroic Materials* (Springer, 2016).
51. P. Giannozzi, S. Baroni, N. Bonini, M. Calandra, R. Car, C. Cavazzoni, D. Ceresoli, G. L. Chiarotti, M. Cococcioni, I. Dabo, A. D. Corso, S. de Gironcoli, S. Fabris, G. Fratesi, R. Gebauer, U. Gerstmann, C. Gougoussis, A. Kokalj, M. Lazzeri, L. Martin-Samos, N. Marzari, F. Mauri, R. Mazzarello, S. Paolini, A. Pasquarello, L. Paulatto, C. Sbraccia, S. Scandolo, G. Sclauzero, A. P. Seitsonen, A. Smogunov, P. Umari, R. M. Wentzcovitch, QUANTUM ESPRESSO: A modular and open-source software project for quantum simulations of materials. *J. Phys. Condens. Matter* **21**, 395502 (2009).
52. G. Kresse, D. Joubert, From ultrasoft pseudopotentials to the projector augmented-wave method. *Phys. Rev. B* **59**, 1758–1775 (1999).
53. I. Hamada, van der Waals density functional made accurate. *Phys. Rev. B* **89**, 121103 (2014).
54. M. J. van Setten, M. Giantomasi, E. Bousquet, M. J. Verstraete, D. R. Hamann, X. Gonze, G.-M. Rignanese, The PSEUDODOJO: Training and grading a 85 element optimized norm-conserving pseudopotential table. *Comput. Phys. Commun.* **226**, 39–54 (2018).
55. D. R. Hamann, Optimized norm-conserving Vanderbilt pseudopotentials. *Phys. Rev. B* **88**, 085117 (2013).
56. P. E. Blöchl, Projector augmented-wave method. *Phys. Rev. B* **50**, 17953–17979 (1994).
57. J. P. Perdew, K. Burke, M. Ernzerhof, Generalized gradient approximation made simple. *Phys. Rev. Lett.* **77**, 3865–3868 (1996).
58. P. Zubko, H. Lu, C.-W. Bark, X. Martí, J. Santiso, C.-B. Eom, G. Catalan, A. Gruverman, On the persistence of polar domains in ultrathin ferroelectric capacitors. *J. Phys. Condens. Matter* **29**, 284001 (2017).
59. P. Debye, E. Hückel, Zur Theorie Der Elektrolyte. I. Gefrierpunktniedrigung Und Verwandte Erscheinungen. *Phys. Z.* **24**, 185 (1923).
60. P. Sharma, S. Ryu, Z. Viskadourakis, T. R. Paudel, H. Lee, C. Panagopoulos, E. Y. Tsymlar, C.-B. Eom, A. Gruverman, Electromechanics of ferroelectric-like behavior of LaAlO_3 thin films. *Adv. Funct. Mater.* **25**, 6538–6544 (2015).

61. R. K. Vasudevan, N. Balke, P. Maksymovych, S. Jesse, S. V. Kalinin, Ferroelectric or non-ferroelectric: Why so many materials exhibit “ferroelectricity” on the nanoscale. *Appl. Phys. Rev.* **4**, 021302 (2017).
62. M. Ahmadi, L. Collins, A. Puzhtov, J. Zhang, J. K. Keum, W. Lu, I. Ivanov, S. V. Kalinin, B. Hu, Exploring anomalous polarization dynamics in organometallic halide perovskites. *Adv. Mater.* **30**, 1705298 (2018).

Acknowledgments: We thank M. Gross (ANFF, UNSW) and H. Nguyen (UNSW) for support with ellipsometry measurements. **Funding:** This research was supported in part by the Australian Research Council Centre of Excellence in Future Low-Energy Electronics Technologies (FLEET), project no. CE170100039, funded by the Australian Government. This work was performed in part using facilities of the NSW Nodes of the Australian National Fabrication Facility. D.Z. acknowledges the Australian Government Research Training Program Scholarship. The research at the University of Nebraska-Lincoln was supported by the National Science Foundation through the Materials Research Science and Engineering Center (NSF grant no. DMR-1420645). **Author contributions:** A.R.H. and F.-X.X. conceived the idea. This idea was developed further by P.S. and J.S. P.S. designed and implemented scanning probe microscopy measurements. F.-X.X. fabricated the WTe_2 samples and

performed the electrical transport measurements. F.-X.X., D.Z., and P.S. performed the XRD structural characterization. D.-F.S. and E.Y.T. conducted and/or analyzed the first-principles DFT calculations. D.Z., P.S., and J.S. collected and/or analyzed the ellipsometry data. P.S. and F.-X.X. wrote the manuscript with input from J.S. and A.R.H. All authors reviewed and contributed to the manuscript preparation. **Competing interests:** The authors declare that they have no competing financial or non-financial interests. **Data and materials availability:** All data needed to evaluate the conclusions in the paper are present in the paper and/or the Supplementary Materials. Additional data related to this paper may be requested from the authors.

Submitted 29 March 2019

Accepted 24 May 2019

Published 5 July 2019

10.1126/sciadv.aax5080

Citation: P. Sharma, F.-X. Xiang, D.-F. Shao, D. Zhang, E. Y. Tsybal, A. R. Hamilton, J. Seidel, A room-temperature ferroelectric semimetal. *Sci. Adv.* **5**, eaax5080 (2019).